Energy dissipation mechanisms during droplet impact on superhydrophobic surfaces

Mehdi H. Biroun,[1] Javad Taghipour,[1] Muhammad Ikhlaq,[1] Jake Howarth,[1] Luca Mazzei,[2] and Yong-Qing Fu[3]
[1)]*Dyson Institute of Engineering and Technology, Tetbury Hill, Malmesbury SN16 0RP, UK*
[2)]*Department of Chemical Engineering, University College London, Torrington Place, London WC1E 7JE, UK*
[3)]*Faculty of Engineering and Environment, Northumbria University, Newcastle upon Tyne NE1 8ST, UK*

(*Electronic mail: Mehdi.Biroun@dysoninstitute.ac.uk)

(Dated: 19 February 2025)

Droplets impacting onto surfaces is a common phenomenon in nature and in various industrial applications, such as bioprinting, wind turbine operations, and spray coating. A detailed understanding of the physics underlying the impact dynamics is critical for these applications. However, capturing the details of this process experimentally and developing analytical models to predict the impact characteristic parameters is a challenge. Here, we present a numerical model designed to simulate the dynamics of droplets impacting superhydrophobic surfaces. Following validation against our experimental data, the model is employed to analyze the energy budget within the liquid phase during impact. Subsequently, a series of simulations are conducted to examine the influences of various physicochemical parameters on droplet impact. Our analysis reveals that energy dissipation during droplet spreading increases linearly with the viscosity, density, and droplet size; conversely, an increased surface tension leads to a lower energy dissipation, while the equilibrium contact angle on superhydrophobic surfaces does not significantly affect energy dissipation during the droplet spreading process. Notably, impact velocity plays a critical role in energy dissipation during spreading. These findings provide detailed insights into mechanisms of energy dissipation during droplet impact which would help in developing more accurate analytical models to predict the droplet impact outcome.

I. INTRODUCTION

One common physical phenomenon we encounter daily is the impact of droplets on solid surfaces. Whether we are traveling in the rain, sneezing into our elbow, watering our plants, or removing a coffee stain from our clothes, we witness droplet-solid interaction. This phenomenon is also critical for many industries and technologies, such as medicine, aerospace, fashion, agriculture, electronics, renewable energy, health-safety-environment, and materials[1–6]. After the pioneering work of Worthington[7] on studying the impact of droplets on horizontal planes, this phenomenon has become an important part of physics and fluid mechanics research.

The droplet impact outcome on a surface is categorized into different impact regimes, including deposition, partial rebound, rebound, jetting, and splashing[8]. The impact behavior of a droplet on a surface involves a series of dynamic processes. At the onset of the impact, a three-phase contact line (TPCL) is formed. When no splashing is observed, the TPCL spreads radially outward until it reaches a maximum spreading diameter D_m. Subsequently, depending on the surface and liquid properties and the impact conditions, the TPCL can either recede or stay close to this maximum spreading region. In cases where the energy dissipation mechanisms dissipate the initial energy of the droplet during the spreading, the droplet remains attached to the surface, a phenomenon known as deposition. Partial rebound occurs when the droplet lacks sufficient energy to fully retract after reaching the maximum spreading diameter. In this case, part of the droplet may separate and rebound, while some liquid remains adhered to the surface. Rebound happens when the droplet has enough energy to complete the receding process and bounce back from the surface nearly entirely. Jetting is observed when a droplet impact leads to the formation of a jet that ejects liquid vertically from the impact point[9].

Surface structure plays a significant role in determining the droplet impact behavior by influencing wettability and energy dissipation rate[10]. Wettability, which governs how a liquid interacts with a solid surface, is primarily determined by the equilibrium contact angle θ_{eq}. A contact angle $\theta_{eq} < 90^\circ$ indicates a hydrophilic surface, on which the liquid spreads more readily. When $\theta_{eq} < 5^\circ$, the surface is classified as superhydrophilic, which means that on it the droplet spreads almost completely. Conversely, a contact angle $\theta_{eq} > 90^\circ$ denotes a hydrophobic surface, where the droplet maintains a more spherical shape. If θ_{eq} exceeds 150° and the contact angle hysteresis $\Delta\theta$ is less than 10°, the surface is considered superhydrophobic[11]. Superhydrophobicity can be achieved by exploiting hydrophobic coatings, increasing surface roughness, and creating air pockets between the solid surface and the droplet[12].
Structured and textured surfaces, such as hierarchical structured surfaces, ribbed or grooved surfaces, slippery liquid-infused porous surfaces (SLIPS), and patterned wettability surface substrates have also been used as a passive method of controlling droplet impact by altering energy conversions during the impact[13–15].

Understanding the dynamics of droplet impact and ultimately the ability to control how droplets interact with solid surfaces is crucial for various industries such as bioprinting[16], inkjet printing[17], forensic science and criminology[18], self-cleaning surfaces[19], and spray cooling[20]. Research has shown

that impact dynamics is influenced by the physicochemical characteristics of the surface, including wettability, texture, and temperature[21], as well as the properties of the liquid, such as density, viscosity, temperature, impact velocity, droplet size, and surface tension[22]. Furthermore, environmental conditions, including temperature, pressure, and humidity, play critical roles in determining the nature of the impact result[23].

In the literature, the maximum spreading radius is one of the parameters that have been used to characterize the impact dynamics[24]. The ability to predict and control the maximum spreading radius is critical for several industrial applications such as spray coating, printing, and spray cooling[25]. However, predicting the normalized maximum spreading ($\beta_m = D_m/D_0$), which represents the ratio of the maximum diameter of a spreading droplet to its initial diameter D_0, is complex. This complexity arises because of the necessity to understand the energy conversions during the spreading phase. Additionally, analysis of β_m becomes more intricate for droplets impacting spherical, structured, or porous surfaces, or under external influences such as magnetic, acoustic, or electric fields[26–28].

Several approaches have been developed to address this complexity, including the momentum balance method[29,30], empirical scaling analysis[31,32], energy budgeting[24], and machine learning methods[33,34]. The momentum balance method involves deriving the equation of motion for the rim surrounding the central lamella of the droplet. Empirical scaling analysis is an empirical, yet highly effective, method for predicting β_m. It involves identifying appropriate scaling relationships that relate β_m to the properties of the liquid and the surface characteristics. The energy budget method analyses how different energy terms convert into each other and evolve during the impact. Unlike the scaling method, which is more empirical, the energy budget method attempts to quantify the precise energy transformations and dissipation mechanisms involved in the spreading process. Machine learning methods commonly use artificial neural networks to predict the maximum spreading based on the available experimental or numerical data. Table I summarizes the important correlations for predicting β_m as a function of different important dimensionless numbers.

To predict the maximum spreading radius, the energy budget method analyses the dynamic interaction between surface energy $E_s(t)$, gravitational energy $E_g(t)$, kinetic energy $E_k(t)$, and energy dissipation $W_{\text{diss}}(t)$ during the impact[35]. In most models, the effect of gravitational energy is ignored, as studies by Biroun et al.[28] and Lee et al.[35] have shown that its impact is less than 3%. In this approach, energy conservation is applied to the fluid domain from the start of the impact to the moment the droplet reaches its maximum spreading radius. The energy conversions can be analyzed using either analytical or numerical methods.

When using analytical methods, one needs to determine the kinetic and surface energy of the droplet at both the onset of impact and maximum spreading, along with the energy dissipation during spreading. Assuming that there is no internal recirculation within the droplet, the kinetic energy at the onset of the impact is given by $E_K(0) = \frac{\pi}{12}\rho D_0^3 U_0^2$, where ρ is the liquid density and U_0 is the impact velocity. Most analytical models assume the kinetic energy becomes zero at maximum spreading, $E_K(t_s) = 0$. This means that the initial energy of the system is either dissipated or stored as surface energy during the spreading. The surface energy at the onset of impact is $E_s(0) = \pi\gamma_{lv}D_0^2$, where γ_{lv} is the surface tension between the liquid and gas phases. The other two factors – energy dissipation during spreading and surface energy at maximum spreading– are more complex, and the accuracy of the models depends on how these terms are calculated. Over the past two decades, several models have been proposed for these terms. Wang et al.[36] provide a table summarizing the correlations for these two terms. Most of these models assume that the shape of the droplet at maximum spreading is a cylindrical or spherical cap[37,38]. However, high-speed imaging and computational fluid dynamics (CFD) results have shown that the shape of the droplet is more complex. Moreover, all these models define correlations for energy dissipation terms as a function of initial droplet properties (such as D_0 and U_0) and the final shape of the droplet at maximum spreading. However, CFD simulations have shown that the internal flows during the spreading are complex. Overall, although several analytical methods have been proposed to predict the maximum spreading of the droplet, and some of these models are effective and simple, there are a lot of uncertainties about the correct definitions and appropriate usage of accurate energy terms.

Over the years, various numerical techniques have been developed to simulate the complex process of droplet impact, each with distinct advantages and limitations. Among these, the Volume of Fluids (VOF) method[47], the Level Set (LS) method[48], the Lattice Boltzmann Method (LBM)[49], and Molecular Dynamics (MD)[50] have been widely employed. For a comprehensive summary of studies utilizing these methods, we refer the reader to the work of Wang et al.[4]. Interface capturing methods, such as VOF and LS, are particularly advantageous due to their high simulation accuracy in capturing free interfaces and their strong adaptability to complex boundary conditions. The VOF method, based on a volume fraction function, effectively satisfies mass conservation, making it suitable for multiphase flow problems with large deformations. The LS method, on the other hand, defines the interface implicitly using a signed distance function, allowing for smooth curvature calculations and facilitating the modeling of topological changes such as droplet merging or breakup[51]. The LBM, a mesoscopic approach, has evolved from the lattice gas model, where particles exist in discrete phase spaces. Based on kinetic theory and the cellular automaton concept, LBM employs simple local update rules based on particle interactions to derive continuous momentum equations[52]. This method is particularly effective for simulating complex fluid behaviors, including interactions with microstructured surfaces and porous media. Recently, MD simulations have been increasingly applied as a microscopic modeling technique. The fundamental principle of MD is that, given the positions of all atoms in a system, the forces acting on each atom due to other atoms can be computed. Using Newtons laws of motion, these forces determine atomic velocities and positions over time, thereby capturing the dynamic behavior of the sys-

TABLE I. Summary of physical models detailing the relationship between the maximum spreading parameter and non-dimensional physical variables *

References	Correlation	Method	Comments
Scheller and Bousfield[39]	$\beta_m = 0.61(\mathrm{Re}^2\mathrm{Oh})^{1/6}$	Empirical scaling analysis	Glycerin aqua mixture liquid impact on polystyrene film and glass surfaces.
Pasandideh-Fard et al.[40]	$\beta_m = \sqrt{\frac{We+12}{3(1-cos\theta_a)+4(We/\sqrt{Re})}}$	Energy Budget Method	Water with sodium dodecyl sulphate (SDS) surfactants droplet impacting on stainless steel surfaces.
Clanet et al.[41]	$\beta_m = 0.9\mathrm{We}^{1/4}$	Empirical Scaling Analysis	The equation is valid for low viscosity droplets impacting on superhydrophobic surfaces.
Ukiwe and Kwok[42]	$(We+12)\beta_m = 8+\beta_m^3(3(1-\cos\theta_{eq})+4We/\sqrt{Re})$	Energy Budget Method	Water and formamide liquid impact on Silicone wafers.
Roisman[30]	$\beta_m \approx 0.87\mathrm{Re}^{1/5}+0.4\mathrm{Re}^{2/5}\mathrm{We}^{-1/2}$	Momentum Balance Method	N.A.
Eggers et al.[29]	$\beta_m \propto Re^{1/5} f_c(WeRe^{-2.5})$	Momentum Balance Method	Two-dimensional (2D) numerical simulation of droplet assuming 180° contact angle at the TPCL.
Seo et al.[43]	$\beta_m = 1.27(\mathrm{Re}^2\mathrm{Oh})^{0.122}$	Empirical Scaling Analysis	Gasoline, Isooctane, and ethanol droplets impacting on an aluminum substrate with an average surface roughness of $0.02\mu m$ with impact velocities between 0.37 and 4.04 m/s.
Aksoy et al.[44]	$\frac{3.18We^{0.75}\beta_m^{6.5}}{Re^{0.86}}+8+3(1-cos\theta_{eq})\beta_m^3 = (We+12)\beta_m$	Energy Budget Method	Glycerol-water solutions impact on smooth sapphire surface. The impact velocity and droplet volume are changed to obtain 294 data points.
Du et al.[45]	$\frac{0.98We^{1.06}\beta_m^{6.5}}{Re}+8+3(1-cos\theta_{eq})\beta_m^3 = (We+12)\beta_m$	Energy Budget Method	2D numerical simulation of glycerol-water solutions impact on smooth surface.
Liu et al.[46]	$(\beta_m^2-\beta_0^2)^{1/2} = \frac{Aln(Re_n^{1/(2n+3)})We^{1/2}}{B+We^{1/2}}$ **	Energy Budget Method	2D finite element numerical simulations on shear-thinning non-Newtonian liquids.

* In this table, $\mathrm{Re} = \rho U_0 D_0/\mu$, $\mathrm{We} = \rho U_0^2 D_0/\gamma_{lv}$, $\mathrm{Oh} = \mu/\sqrt{\rho\gamma_{lv}D_0}$ are the non dimensional numbers. θ_a is the advancing contact angle of the droplet on the surface.

** A and B are fitting coefficients; and β_0 is defined as a function of surface wettability properties[46].

tem at an atomic level. MD enables the precise resolution of molecular-scale interactions, making it particularly useful for investigating droplet spreading, granular flow dynamics, and hydrophobicity[53–55]. However, a significant drawback of this model lies in its high computational cost. This limitation renders the approach particularly impractical for studies requiring extensive sensitivity analyses or optimization processes, as these demand a large number of simulations.

Lately, multiscale hybrid simulations have emerged as a powerful approach to capturing droplet interactions with solid surfaces. This method integrates macroscopic fluid dynamics with microscopic interfacial effects, linking continuum models, like VOF, with atomistic or mesoscopic techniques, like MD. By incorporating small-scale wetting phenomena and molecular forces into large-scale flow simulations, this approach offers a more comprehensive representation of droplet behaviors, including spreading, bouncing, and splashing[56,57].

All numerical methods provide a useful tool for calculating the various energy terms during impact. CFD results offer detailed information, allowing for a more accurate definition of surface energy both during spreading and at maximum spreading. Additionally, they enable the tracking of cumulative energy dissipation throughout the impact. As a result, numerical simulations allow a better understanding of the overall energy conversions during the impact. In these simulations, the time-dependent kinetic energy of the droplet is computed as the integral of the local kinetic energy per unit volume of fluid over the droplet volume at a given moment in time[48]:

$$E_k(t) = \frac{1}{2}\rho \int_V |\mathbf{U}|^2 dV \tag{1}$$

where $|\mathbf{U}|$ is the magnitude of the local velocity of the liquid phase. Although gravitational energy is negligible during the impact, in CFD simulations, it is accounted for. The time-

dependent total gravitational energy of the droplet is given by:

$$E_g(t) = \rho g \int_V z dV \tag{2}$$

where z is the distance of the fluid element from the solid wall in the direction parallel to the gravitational acceleration vector, and g is the magnitude of the gravitational acceleration. The time-dependent surface energy at each moment is given by:

$$E_s(t) = \gamma_{lv} S_a + \gamma_{ls} S_s \tag{3}$$

where S_a and S_s are the areas of the droplet in contact with the surrounding gas and the solid surface, respectively[36], and γ_{ls} is the surface tension between the liquid and solid phases. The cumulative energy dissipation from the onset of the impact until time t is given by:

$$E_{\text{diss}}(t) = \int_0^t \int_V \phi_{diss} dV ds \tag{4}$$

where s is a dummy integration variable (for the time integration) and ϕ_{diss} is the viscous dissipation function; this represents the kinetic energy irreversibly converted into internal energy per unit time and volume and is given by[58]:

$$\phi_{\text{diss}} = 2\mu(\mathbf{S}_{ij} \cdot \mathbf{S}_{ij}) \tag{5}$$

where $\mathbf{S}_{ij} \equiv \frac{1}{2}[(\nabla \mathbf{U} + (\nabla \mathbf{U})^T)]$ is the strain rate tensor, and μ is liquid viscosity.

Numerical methods have the potential to provide deeper insights into spreading dynamics and illustrate the fluid behavior in more detail during spreading[46]. The level of detail these models can offer is critical for refining and improving the accuracy of existing analytical methods that predict key droplet impact parameters. While some research exists on energy budget analysis of droplet impact using numerical methods, a systematic energy budget analysis has not yet been carried out. This systematic analysis could be a crucial tool for advancing analytical approaches and clarifying the effects of various variables on critical impact parameters such as contact time and spreading time.

For example, the spreading time t_s in droplet impact dynamics is crucial as it governs impact outcomes, surface wetting, coating uniformity, environmental influence, and secondary process efficiency, making it essential for optimizing applications such as cooling, printing, and material coatings[59]. Hao et al. suggested that the spreading time for bouncing droplets should ideally comprise only about 20-30% of the total contact time[60]. Pasandideh-Fard et al.[40] proposed the simple analytical model $t_s = 8D_0/3U_0$, where the spherical droplet was assumed to spread into a cylindrical disk. However, this simple method did not consider the liquid and solid surface properties. Experimental results by Liang et al have shown that t_s depends on the surface tension and viscosity of the liquid, and on the surface roughness.[61]. Numerical and experimental findings by Lee et al.[35] demonstrated that higher impact velocities correlate with shorter maximum spreading times. Moreover, surface tension exhibits an inverse relationship with maximum spreading time, as increasing surface tension at constant impact velocity results in a lower maximum spreading time[62].

The contact time of a droplet, which refers to the duration from its initial landing on a surface to its complete rebound, has been extensively studied. In 2002, Richard et al.[63] conducted research on droplets impacting onto superhydrophobic surfaces, discovering that the contact time was independent of the impact velocity. They derived a classical equation to estimate the contact time, $t = a\left(\rho D_0^3/8\gamma_{lv}\right)^{1/2}$. Here, a is an experimentally determined prefactor. This equation implies that the droplet size, rather than the impact velocity, primarily influences the contact time. Numerous studies have corroborated this scaling equation, with a typical value of a approximately equal to 2.6 for common non-textured superhydrophobic surfaces[63].

While numerous studies have utilized numerical models to analyze droplet impact, there remains a significant gap in understanding the effects of critical parameters on energy conversions during the impact. In this study, we develop and implement a numerical model to simulate droplet impact on superhydrophobic surfaces. Following the model development, we validate the model using our experimental data. Subsequently, we conduct a comprehensive CFD simulation campaign, systematically varying key parameters including contact angle, liquid viscosity, density, impact velocity, surface tension, and droplet size. By varying one parameter at a time while keeping all others constant, we isolate and analyze the specific effects of each variable on the impact dynamics. This approach allows examining in detail individual factors, a challenge often encountered in experimental settings where parameter interdependency complicates analysis. The findings from this research provide valuable insights into the role each variable plays in the energy budget and impact characteristics on superhydrophobic surfaces.

II. EXPERIMENTAL SETUP AND MATERIALS

A. Droplet Impact Experimental Setup

The experimental setup for droplet impact analysis consisted of a high-speed imaging system designed to capture the dynamics of the impact. The impact was recorded from a side view using a Photron Nova S6 high-speed camera equipped with a Laowa 100 mm F2.8 2:1 Ultra Macro APO lens. The camera was operated at 7200 frames per second with a shutter speed of 1/30000 seconds and a resolution of 1024×512 pixels. A 100 W LED chip white lighting system with fan cooling, providing 10000 lumens of light, was used as the backlight for the imaging system. The backlight was positioned 10 cm behind the impact area, and a light filter was placed between the light source and the impact zone to enhance contrast and clarity. Calibration of the camera was performed using a 2 cm calibration piece. The recorded surface shape is highly defined and can be readily analyzed using image processing techniques. Deionized (DI) water droplets were

generated from a 27 gauge needle (Adhesive Dispensing Ltd.) mounted on a three-dimensional (3D) positioner. To measure the size of the generated droplets, 10 droplet impact experiments were recorded, and the droplet radii were measured. The average droplet volume was calculated to be 5.76 μl, with a standard deviation of 0.044 μl. The droplets were released from a height of 100 mm, with an initial velocity of zero, reaching an impact velocity of 1.4 m/s upon contacting the surface. The impact tests were conducted under atmospheric conditions, with an ambient temperature of $21 \pm 0.5^{\circ}C$ and a relative humidity of $30 \pm 1\%$. Each impact test was repeated four times to ensure the repeatability and consistency of the experimental results.

B. Surface Treatment and Characterization

Glass slides were treated with silica nanoparticles suspended in isopropanol (IPA) (Glaco Mirror Coat Zero from Soft99 Co.) to achieve superhydrophobicity. This process involved spraying the particles five times onto the surface after allowing the IPA to evaporate, resulting in a porous layer approximately 2 μm thick. Previous studies using the same coating indicated a surface roughness of 0.07 μm[15].

To characterize the surface properties, the contact angles of water were measured using a drop shape analyzer (Theta Lite, Biolin Scientific Ltd.). The measurements included advancing and receding contact angles, as well as contact angle hysteresis, defined as the difference between advancing and receding contact angles. Droplets of fixed volume (5.7 μl) were used for these measurements. The equilibrium, advancing, and receding contact angles for this surface are 162.0°, 163.7° and 161.7°, respectively, making the contact angle hysteresis of 2° (See FIG. 1(a)).

C. Surface Inspection

To verify the quality of the surface coating, a scanning electron microscope (SEM, JEOL 7900F) was used to observe the surface morphology of the coated glass slide. To minimize the image distortion caused by charging, a thin layer of gold was deposited on the slide using an Agar Scientific Sputter Coater with a chamber pressure of 0.03 mbar, and a current of 30 mA for 20 s. FIG. 1(b) shows one of the obtained SEM images of coatings.

III. NUMERICAL METHODS

A. Mathematical Model

To simulate the droplet impact scenarios, we employed the interFoam solver from the OpenFOAM-9.0 CFD package[64]. The interFoam solver is based on the Volume of Fluid (VOF) multiphase flow model to accurately capture the liquid-gas interface during the impact process. For an isothermal and incompressible system with no phase change, the governing

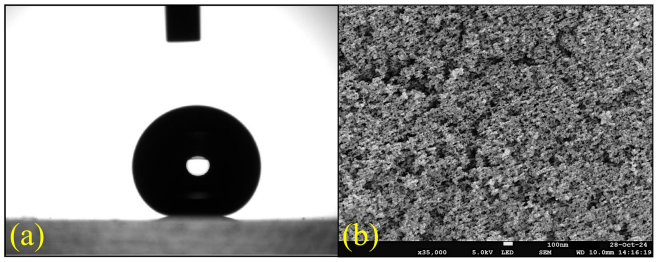

FIG. 1. (a) Equilibrium Contact angle of the droplet on the superhydrophobic surface, (b) SEM image of the coated surface.

equations include the continuity and linear momentum balance equations, which read[65]:

$$\nabla \cdot \mathbf{U} = 0 \tag{6}$$

$$\rho[\frac{\partial \mathbf{U}}{\partial t} + \nabla \cdot \mathbf{U}\mathbf{U}] = -\nabla p + \nabla \cdot \mathbf{T} + \rho \mathbf{g} + \mathbf{F}_s \tag{7}$$

where p and $\mathbf{T}$ are the pressure and deviatoric stress tensor of the liquid-gas mixture, respectively. Since the fluid is assumed to be Newtonian, we have that $\mathbf{T} = \mu \left[\nabla \mathbf{U} + (\nabla \mathbf{U})^T\right]$. In Equation (7), $\rho \mathbf{g}$ is the gravitational body force, and $\mathbf{F}_s$ is the surface tension force. The liquid volume fraction at each spatial point occupied by the gas-liquid mixture is denoted by α. Thus, α varies between zero and one in the liquid-gas interface region, being zero in the gas phase and one in the liquid phase. This evolution equation for this variable is [65]:

$$\frac{\partial \alpha}{\partial t} + \nabla \cdot \alpha \mathbf{U} = 0 \tag{8}$$

The two immiscible fluids are treated as a single fluid (the mixture) throughout the entire domain. The physical properties of this fluid are calculated as weighted averages, based on the liquid volume fraction. This approach ensures that the properties correspond to those of each fluid in the regions they occupy, with variations occurring only at the interface between the two phases[65].

$$\rho = \rho_l \alpha + \rho_g (1 - \alpha) \tag{9}$$

$$\mu = \mu_l \alpha + \mu_g (1 - \alpha) \tag{10}$$

The properties of the liquid and gas are denoted by l and g subscripts, respectively. To close Equation (7) an expression is needed for the surface tension force per unit volume:

$$\mathbf{F}_s = \gamma_{lv} \kappa \nabla \alpha \tag{11}$$

where κ is the interface curvature, given by:

$$\kappa = -\nabla \cdot \left(\frac{\nabla \alpha}{|\nabla \alpha|} \right) \tag{12}$$

B. Boundary Conditions

In this simulation, appropriate boundary conditions were defined for the liquid volume fraction, pressure, and velocity fields to accurately model the droplet impact on a superhydrophobic surface. For the liquid volume fraction, a `constantAlphaContactAngle` condition was applied at the bottom boundary. This boundary condition modifies the surface tension force in the vicinity of the TPCL to account for the pinning forces present at the TPCL[66]. Specifically, in regions occupied by a single phase (i.e., where $\alpha = 0$ or $\alpha = 1$), the gradient of the phase fraction field α is set to zero, ensuring no spurious contributions to the force. In contrast, for regions where $0 < \alpha < 1$, the gradient $\nabla\alpha$ is computed directly based on the specified equilibrium contact angle by:

$$\nabla\alpha = \mathbf{n}_{\text{wall}}.\cos(\theta_{eq}) \tag{13}$$

where $\mathbf{n}_{\text{wall}}$ is the normal vector to the wall face which is perpendicular to the face pointing outward from the cell it belongs to. For further details, readers are referred to[47,67]. Although the contact angle hysteresis is very low for this case, it can still generate local pinning forces at the TPCL. To thoroughly investigate its influence, we tested the effect of contact angle hysteresis on impact dynamics and energy dissipation. This allowed us to understand how even minimal hysteresis could affect the behavior of the droplet upon impact and the resulting energy distribution. To do this, we carried out one simulation with the same simulation setup and applied the `DynamicAlphaContactAngle` boundary condition for liquid volume fraction at the solid wall. This boundary condition is more sophisticated as it considers contact angle hysteresis to calculate a more accurate local contact angle. The calculation of the local contact angle is based on the velocity of the TPCL and the properties of the surface. By incorporating these additional factors, the `DynamicAlphaContactAngle` boundary condition becomes more precise. As expected, this extra accuracy comes with higher computational costs. Comparing simulations with both boundary conditions, we noticed negligible differences in results and relatively higher computational costs when using the `DynamicAlphaContactAngle` boundary condition. Thus, to reduce computational costs, we opted to use the `ConstantAlphaContactAngle` boundary condition for all simulations. For all other boundaries, the `zeroGradient` was used for the liquid volume fraction.

The pressure boundary conditions consist of a `fixedFluxPressure` at the solid wall. The `fixedFluxPressure` boundary condition is typically applied in a way that relates the pressure gradient to the specified pressure flux. The general form of this boundary condition can be expressed mathematically as:

$$\phi_p = \mathbf{n}_{wall}\nabla p \tag{14}$$

where ϕ_p is the pressure flux, which is set to zero in this simulation. The sides and top boundary conditions in the mesh are assigned `totalPressure` conditions. This boundary condition is a fixed value condition calculated from atmospheric pressure and local velocity. The `totalPressure` boundary condition is used to set the static pressure at a surface p_p, based on subtracting the dynamic pressure from the total pressure p_0 as:

$$p_p = p_0 - \frac{1}{2}|\mathbf{U}|^2 \tag{15}$$

For the velocity, a `no-slip` ($\mathbf{U} = 0$) condition was applied at the solid wall boundary to model realistic friction between the fluid and the surface. For the sides and top boundary conditions, a `pressureInletOutletVelocity` condition was used, which in OpenFOAM is suitable for boundaries where the fluid flows in or out of the the control volume. The mathematical formulation of this boundary condition for outflow (where the fluid is leaving the domain), is a zero-gradient velocity condition and for inflow (where the fluid is entering the domain), the velocity is set to a specified inlet value:

$$\mathbf{U} = \mathbf{U}_{inlet} \tag{16}$$

where $\mathbf{U}_{inlet}$ is the inlet velocity at inlet patches, which can be defined. In our case, this velocity was set to zero.

C. Numerical Setups

Since the flow is low-speed (the Reynolds number is below 200 in all simulations) and incompressible, we employed the PIMPLE algorithm, which combines PISO (Pressure Implicit with Splitting of Operators) and SIMPLE (Semi-Implicit Method for Pressure-Linked Equations) algorithms for the pressure-velocity coupling. The PIMPLE method was configured with three inner correctors and no momentum prediction, ensuring efficient pressure-velocity coupling for transient simulations. A smoothSolver with symmetric Gauss-Seidel smoother was used for the velocity field to achieve convergence with a tolerance of 10^{-7}. The pressure correction equations were solved using a Preconditioned Conjugate Gradient (PCG) solver with GAMG (Geometric-Algebraic Multi-Grid) preconditioning, ensuring stable and efficient convergence with a tolerance of 10^{-9} and a relative tolerance of 0.05.

The simulation used Euler time-stepping for time discretization, and for spatial discretization, Gauss linear schemes were applied for gradient and laplacian terms, while a limitedLinear scheme was used for the divergence of convective terms. The interface compression scheme, vanLeer, was employed for capturing the droplet-gas interface, ensuring sharp phase boundaries. The time step was dynamically adjusted using a maximum Courant number of 0.3 and maximum alpha Courant number of 0.3, with a time step size limited to a maximum of 10^{-3} s.

D. CFD Simulation Case Setup

Since the goal of this research is to capture the energy budget during droplet impact in detail, all simulations were conducted in 3D. The computational domain for all cases was a

rectangular box with dimensions of $3D_0 \times 3D_0 \times 3D_0$ along the X, Y, and Z-directions in Cartesian coordinates. In all the simulations the gravitational vector is set to be in the **k** direction, where **k** is the unit vector in the Z-direction. In the VOF method, air was treated as the primary phase and the droplet as the secondary phase, with no mass transfer occurring at the interface between the two immiscible fluids. Air properties were kept constant in all simulations, with the viscosity set to 1.552 $\times 10^{-5}$ kg/(m·s) and the density at 1.1839 kg/m^3. In the standard cases (where the density, surface tension, and viscosity of water were not altered for research purposes), the viscosity of water was maintained at 9.74×10^{-4} kg/(m·s), the surface tension was kept constant at 0.072 N/m, and the density at 999.13 kg/m^3. Since the Reynolds number in droplet impact cases remains relatively low, all simulations were carried out for laminar flow and without considering any turbulence model. All simulations were carried out in parallel on one Intel Xeon Gold 6248 2.50 GHz (36 cores) processor.

IV. RESULTS AND DISCUSSION

A. Experimental Results

In this section, we first present the experimental results and explain the observations. These results are then used in the next section to validate the CFD simulations. A set of four impact experiments was conducted with water droplets having an initial impact velocity of $U_0 = 1.4$ m/s and a volume of 5.76 μl. The impact velocity in the experiments was determined by dividing the displacement of the droplets bottom edge in the final two frames before impact by 1.39×10^{-4} s, which represents the time interval between frames. The average impact velocity was found to be 1.404 m/s, with a standard deviation of 0.012 m/s. The mean contact time observed in the experiments was 10.935 ms, with a standard deviation of 0.182 ms. Additionally, the average time to reach the maximum spreading radius was 2.5 ms, with a standard deviation of 0.14 ms. The average normalized maximum spreading radius was 2.51, with a standard deviation of 0.24. FIG. 2 shows snapshots of a droplet impacting the superhydrophobic surface. After the initial impact, the droplet rim spreads outward. As shown in FIG. 2, the actual maximum spreading radius is greater than the radius in contact with the solid surface. In this study, we refer to the maximum spreading radius as the radius on the solid surface. At 2.5 ms after impact, the droplet reaches its maximum spreading radius, after which the rim begins to retract toward the impact point. Due to the high quality of the surface coating, no local disruptions are observed during the spreading phase, and the droplet maintains a relatively symmetrical shape during retraction. A surface with poor coating quality would likely result in local inconsistencies in the spreading and receding contact angles, altering local velocities and distorting the droplet shape during retraction. This would lead to a non-vertical jet formation. The time between the maximum spreading and the droplet detachment from the surface can be divided into two phases: the retraction phase, and the jet formation and separation phase. During the retraction phase (2.5 - 5.3 ms), the droplet rim moves inward toward the impact point without forming a jet. After 5.3 ms, a jet begins to form from the impact point, moving upward with an average velocity of about 1.88 m/s. Finally, after 11.25 ms, the droplet separates from the surface.

B. Mesh Independence tests

The first step in the CFD simulations was to conduct mesh independence tests. Before experimental validation, we simulated a droplet impact with an impact velocity of 1.4 m/s and an initial droplet volume of 5.76 μl. A Cartesian cubic mesh was generated using OpenFOAM's `blockMesh` tool, and the grid size Δx was varied from $\Delta x = D_0/30$ to $\Delta x = D_0/60$. The droplet was initialized adjacent to the surface using the `setFields` utility, with the velocity field set to the impact velocity in the direction of gravity.

As shown in Table II, simulation results indicated that for mesh sizes smaller than $\Delta x = D_0/50$, the maximum spreading radius remained relatively unchanged. Therefore, all simulations in this study were performed with a mesh size of $\Delta x = D_0/50$.

TABLE II. Results of mesh independence tests

$\Delta x/D_0$	1/30	1/40	1/50	1/60
β_m	2.319	2.355	2.372	2.373

C. Model Validation

The next step in the analysis is to compare the experimental and simulation results to test the accuracy of the numerical model. For this comparison, we quantitatively examine two key impact characteristics: the normalized spreading radius, $\beta = d/D_0$, and the normalized maximum height of the droplet, $\eta = h/D_0$, as shown in FIG. 3. In the simulations, the width of the contact area between the droplet and the solid surface is used to define the spreading radius. The embedded illustration in FIG. 3 shows how these parameters are measured and calculated. FIG. 3 demonstrates good qualitative agreement between the experimental and numerical results.

Next, we analyze the relative error between experimental and simulation results. At the end of the spreading phase, where β reaches its maximum value, the results show a relative error of -5.5% for β, while η exhibits a notably larger relative error of -39.8%. Note that a negative value of the relative error means underestimation by the numerical model. Although the value of η calculated by the numerical model is very close to the experimental value, the large relative error is due to the small value of η at this point. At the end of the retraction phase ($t = 5.1$ ms), the relative error for β shifts to +9.7%, and that for η reduces considerably to -2.1%. The maximum relative error for β during the first 5.1 ms (i.e., spreading and retraction phases) is +16%. As evident in FIG.

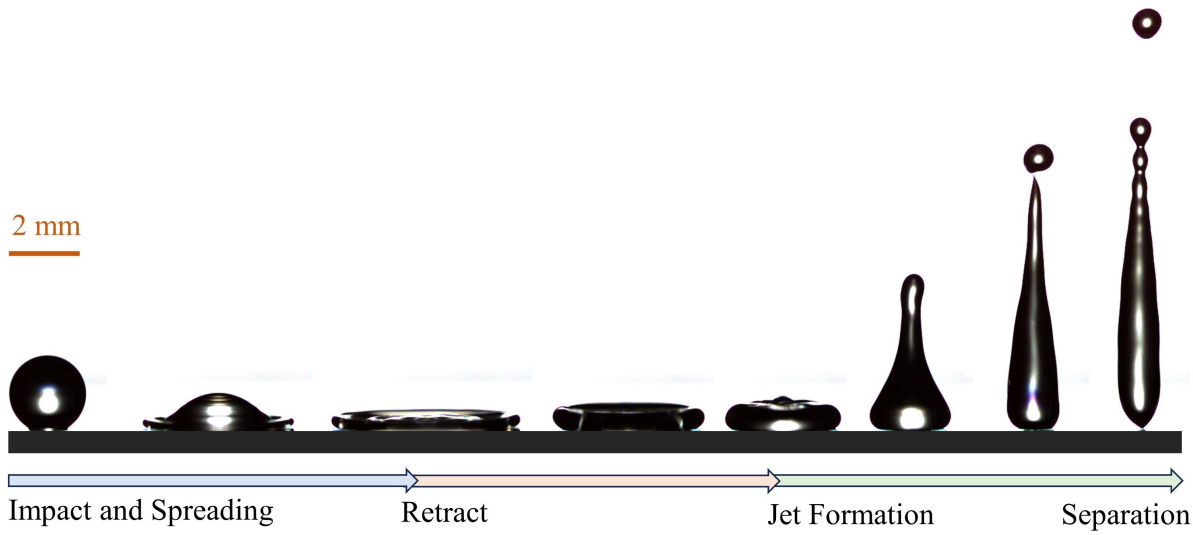

FIG. 2. Snapshots of water droplet impact on the Glaco-coated superhydrophobic surface. In experiments, a droplet with a volume of 5.76 μl impacts the solid surface with a velocity of 1.4 m/s.

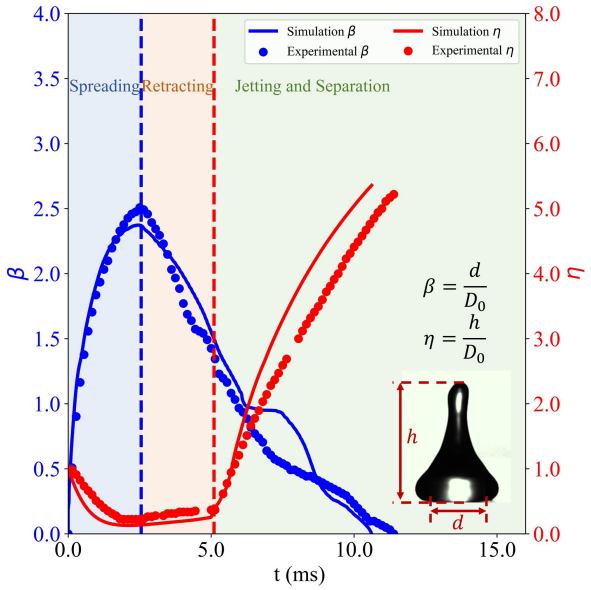

FIG. 3. Temporal evolution of the normalized spreading radius and normalized maximum height of the droplet during the impact. In experiment and simulation, a droplet with a volume of 5.76 μl impacts the solid surface with a velocity of 1.4 m/s.

3, a considerable difference between the experimental and numerical results for β is observed between 6.8 ms and 8.6 ms after the onset of the impact. During this period, β experiences an average error of +56.9% and a maximum error of +72.9%. Meanwhile, η maintains a relatively constant error, averaging +26.0% and reaching a maximum of +27.7% during the final stages of jetting and separation (6.8-11 ms after the onset of impact).

FIG.4 presents the numerical results for the temporal evolution of the droplet interface during impact. In these snapshots, the internal flows within the droplet are shown from the XZ-midplane with velocity vectors. At the onset of impact, assuming no internal recirculation within the droplet, all velocity vectors point in the Z-direction. As the impact progresses, while the liquid at the top of the droplet continues moving downward, a secondary radial flow toward the rim of the droplet is generated. The momentum generated by this flow overcomes surface tension, deforming the droplet interface. As spreading continues, the flow toward the rim becomes dominant within the droplet. An interesting phenomenon occurs when the droplet reaches its maximum spreading radius. The snapshot at 2.4 ms clearly shows that a flow towards the rim is still present, and regions with lower droplet thickness exhibit higher velocity magnitudes. This shows that the assumption in analytical models for zero kinetic energy at the maximum spreading moment is not completely accurate. After the maximum spreading radius has been reached, the surface tension forces begin to pull the droplet's rim back toward the impact point, generating momentum in that direction. Snapshots at 5.0 ms and 6.8 ms show that the flow converges at the impact point and pushes upward, forming a jet. This momentum continues to push the droplet upward until it detaches from the surface. A subunit separates from the main droplet body due to the occurrence of Reynolds-Plateau instabilities, a phenomenon characterized by the breakup of liquid structures when the surface tension forces cannot hold the elongated shape, leading to the formation of small droplets.

D. Energy Budget Analysis

The graph in FIG. 5 shows the temporal evolution of the energy terms during the impact of a droplet. The total en-

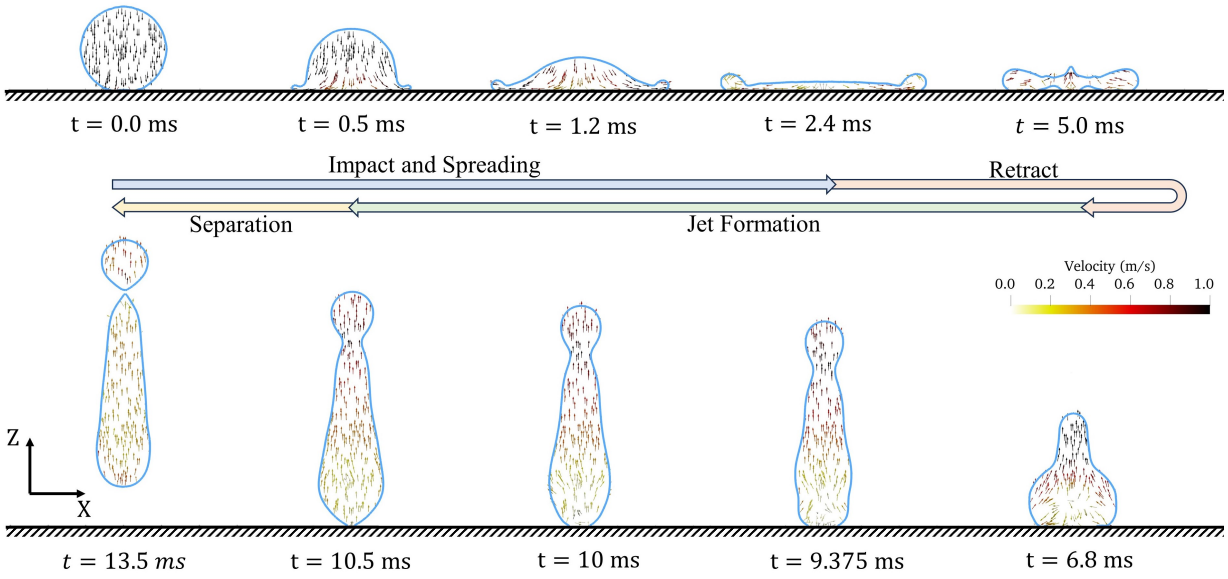

FIG. 4. Numerical results showing Snapshots of droplet XZ-midplane overlaid by the velocity vector magnitudes. In this simulation, a droplet with a volume of 5.76 μl impacts the solid surface with a velocity of 1.4 m/s.

ergy of the droplet at any moment is the sum of the surface, gravitational, and kinetic energies. It is apparent that the variation of the gravitational energy during the impact is negligible. Therefore, in the analysis in this section, this energy term is ignored. Once the droplet hits the solid surface, a series of energy conversions start to happen, which determine the impact outcome. For this impact scenario, initially, the droplet has approximately 80% of kinetic energy and 20% of surface energy. Immediately after the impact and while the droplet spreads, a part of the kinetic energy converts into surface energy, but most of it dissipates into internal energy. FIG. 5(b) shows that during the spreading phase and subsequently during the beginning of the retraction phase (that is, during the first 4 ms of the impact), approximately 65% of the initial total energy of the droplet dissipates. This is mainly due to the change in direction of the initial momentum, which occurs owing to the interaction between the liquid phase and the solid phase. This direction change generates internal recirculation and in turn velocity gradients, which dissipate kinetic energy owing to the viscous stresses arising in the liquid phase. Besides, the interaction between the solid surface and the liquid is another major source of energy dissipation. The no-slip boundary condition causes a high velocity gradient between the stationary wall and the liquid which causes high viscous stresses in the wall region which in turn dissipate the kinetic energy.

On the other hand, the initial surface energy of the droplet slightly decreases at the start of the impact for approximately 0.5 ms, and then starts to rise sharply since the droplet spreads on the surface and its surface area increases. An interesting observation, which is not easy to capture in experiments, is that the surface area of the droplet continues to increase (for another 0.5 ms) even after the radius of the droplet has reached its maximum value (at t = 2.5 ms). This is because, although maximum spreading is achieved, the internal surface of the droplet, which is covered by the droplet rim and not observed in experimental videos, continues to increase at the start of the retraction. The surface energy then starts to convert back into kinetic energy, which triggers the retraction phase, and the droplet begins jetting into the air. Notably, during the jetting phase, the energy dissipation is minimal since there is no change in the direction of the internal flows, and internal recirculation is not observed in the droplet. During the jetting phase, all the velocity vectors are upward and rather parallel (see FIG. 4).

FIG.5(a) illustrates the concept of a mass-spring-damper system, providing a simplified representation of energy conversion during droplet impact. In this analogy, three components are considered: the spring stiffness k_{eff} represents surface energy, the two masses embody the kinetic energy of the droplet (owing to both translational and relative motion), and the coefficient damper c_{eff} models the energy dissipation within the droplet due to liquid viscosity. Including two masses in the model simulates the velocity field inside the droplet and the overall motion of the droplet. This helps to represent the surface energy variation and energy dissipation within a droplet. The arrows beside each mass denote the directional velocity of the mass, starting from U_0, the initial velocity of the droplet just before the impact. At the outset of impact, the mass-spring-damper system possesses both kinetic and potential (surface) energy, where the kinetic energy is mainly due to the translational motion of the whole system; i.e., both masses are assumed to have the same velocity U_0 gained from free fall, as shown in FIG. 5(a). In this instance, the kinetic energy due to the translational energy dominates the internal kinetic energy. On the other hand, the potential (surface) energy is related to the initial deflection of the spring which is $\sim 20\%$ of the total initial energy of the droplet

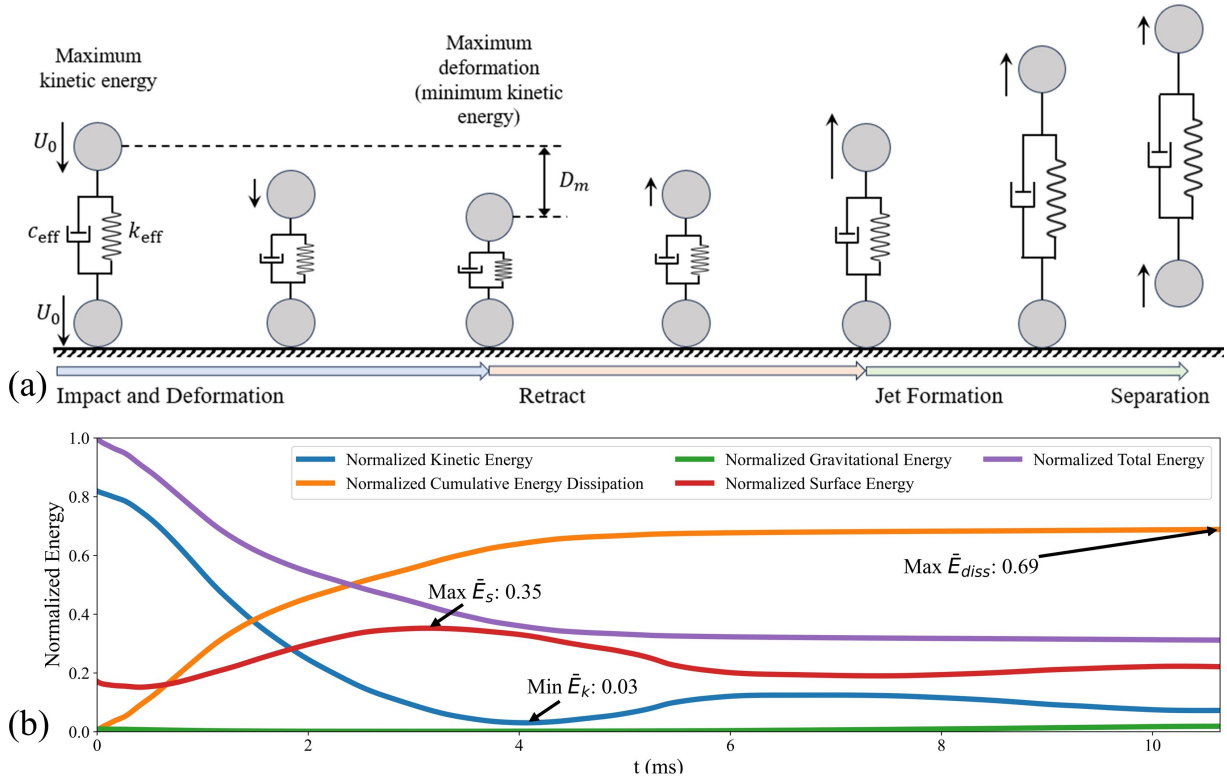

FIG. 5. (a) Schematic illustration of the mass-spring-damper system to explain the energy budget of the droplet. (b) Temporal evolution of the energy terms during the impact. In this simulation, a droplet with a volume of 5.76 μl impacts the solid surface with a velocity of 1.4 m/s.

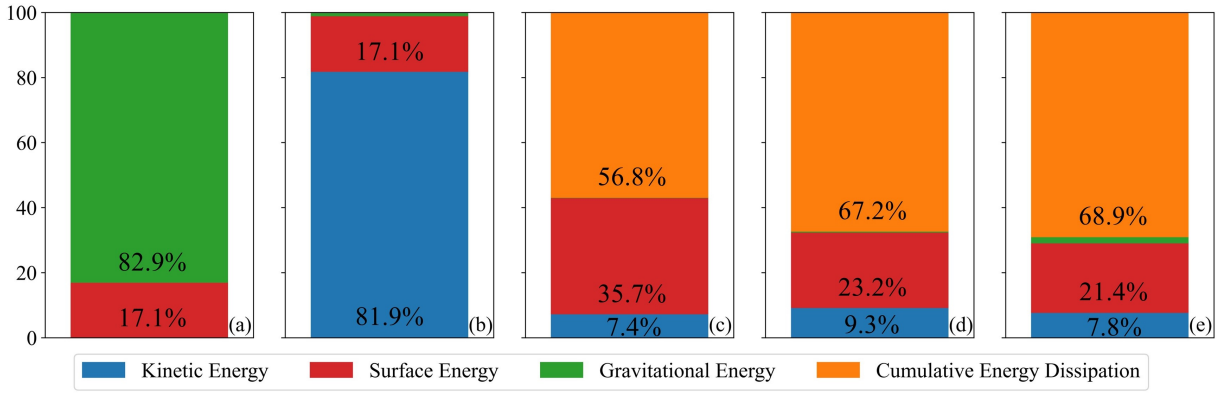

FIG. 6. Breakdown of normalized energy terms during different stages of droplet impact: (a) release from the initial height, (b) onset of impact, (c) reaching maximum spread, (d) beginning of jet formation, and (e) separation from the solid surface. In this simulation, a droplet with a volume of 5.76 μl impacts the solid surface with a velocity of 1.4 m/s.

(See FIG. 5(b)). After impact, the droplet spreads on the solid surface and internal recirculation generates within the droplet. Therefore, the viscous stress (damper) starts to dissipate energy. Additionally, the spring compression increases the amount of potential (surface) energy in the system.

Once the droplet reaches its maximum deformation (see FIG. 5(a)), the kinetic energy holds its minimum value (there is some internal kinetic energy within the droplet which prevents the kinetic energy from being zero). Then, the retraction process starts with the spring releasing its potential energy and the upper mass regaining its momentum in the upward direction. This continues until the end of the retraction process when the droplet takes on (almost) its initial shape. The upper mass which has gained an upward velocity will cause the spring to be deflected in the opposite direction (in a real droplet this will be the vertical spread of the droplet compared to an initial horizontal spread during the impact), starting the jet formation process. The deformation of the spring contin-

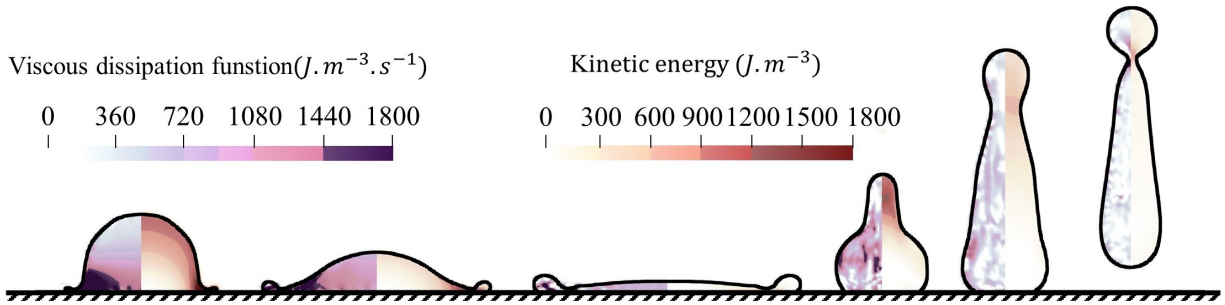

FIG. 7. Temporal evolution of the droplet XZ-midplane, overlaid with contours of the energy dissipation function and kinetic energy. In this simulation, a droplet with a volume of 5.76 μl impacts the solid surface with a velocity of 1.4 m/s.

ues until the lower mass starts gaining upward velocity. When this happens, the whole droplet separates from the substrate.

FIG. 5 (b) shows the energy variation of the droplet from the beginning of the impact process until the droplet separates from the substrate. Initially, the total energy of the droplet is shown to consist of the kinetic energy (approximately 80%) and the surface energy (approximately 20%) of the droplet. At the outset of the impact, as the droplet starts deforming, the internal motion of the droplet causes the damping to dissipate the energy of the droplet. As expected, the energy dissipation rate reaches its maximum during the initial moments of the impact (approximately 1 ms after the start of the impact) when internal recirculation is maximum (See velocity vectors in FIG. 4). About 69% of the initial total energy of the droplet has dissipated when the droplet completes the impact and detaches from the substrate.

FIG. 6 illustrates the breakdown of the various energy terms during the different stages of the droplet impact. Initially, when it is generated, the droplet possesses internal kinetic energy owing to the internal fluid recirculation resulting from the flow within the syringe and the needle during the droplet generation process. We assume that the time between the generation of the droplet and the beginning of the droplet impact on the solid surface is sufficient for this internal kinetic energy to fully dissipate. Consequently, in our analysis, we completely neglect this contribution. Accordingly, at the point of release, we assume that the droplet only possesses gravitational and surface energy. As the droplet falls, its gravitational energy gradually converts into kinetic energy; by the onset of impact, this conversion reaches approximately 99%. During the droplet free fall, we assume that no internal fluid recirculation generates; this assumption is reasonable, because the free fall duration is insufficient to generate significant internal recirculation. During the spreading phase, 56.8% of the initial total energy of the droplet dissipates. The surface energy increases from 17.1% to 35.7% as a result of the increased total surface area of the droplet. In the retraction phase (that is when going from FIG. 6 (c)-(d)), the surface energy decreases by 12.5%, with 1.9% converting back into kinetic energy and the remainder being dissipated. During the jet formation phase (that is when going from FIG. 6 (d)-(e)), the surface energy continues to gradually diminish; additionally, kinetic energy reduces by 1.5%, while the gravitational energy increases by 1.9% as the droplet rises from the surface.

FIG. 7 presents the temporal evolution of the spatial profiles of the energy dissipation function (left side) and of the kinetic energy (right side) of the droplet in the XZ-midplane (See FIG. 4 for coordinates definition) during the impact. This figure illustrates the regions within the droplet where significant energy dissipation occurs throughout the impact process. During the spreading phase, the kinetic energy of the droplet is concentrated near the liquid-gas interface. Due to the no-slip boundary condition at the solid surface, regions close to the wall and impact point exhibit minimal velocity, resulting in lower kinetic energy levels, as shown in the first two snapshots. However, in the droplet rim, the highest concentration of kinetic energy is observed since the droplet is spreading in that region. As the droplet reaches its maximum spreading radius, the kinetic energy contours nearly fade, indicating a decrease in kinetic energy across the main body. However, in the narrow region connecting the main droplet body to the rim, flow persists, and kinetic energy remains present. During this spreading phase, energy dissipation is primarily due to internal recirculations and velocity gradients, particularly near the solid surface and at the droplet rim. In the rim region, as flow reaches the liquid-gas interface and reverses inward, a recirculation zone forms, leading to high rates of energy dissipation. As depicted in FIG. 5, even at maximum spreading, energy dissipation remains significant within the rim region.

In the retraction and jet formation phases, the surface energy converts back into kinetic energy. Therefore, the kinetic energy inside the liquid starts to recover. This recovery is evident near the jet tip, where kinetic energy is higher pushing the droplet upward, while regions close to the solid surface exhibit lower kinetic energy. Despite the decreased rate of energy dissipation during retraction compared to spreading, local gradients and internal recirculations within the droplet continue to dissipate energy. These observations demonstrate the capability of the CFD simulations to reveal detailed impact dynamics, such as energy dissipation patterns and internal flow structures, which are challenging to capture in experimental studies.

E. Sensitivity Analysis

In this section, we apply the developed numerical model to conduct a sensitivity analysis examining the effects of various physicochemical properties of droplets on key impact parameters. First, we established a baseline, referred to as the *standard case*, which provides reference values for comparison. Six sets of CFD simulations were then performed, with each set isolating and varying one parameter while keeping all others constant at their *standard case* values. The parameters examined in this study include liquid density, viscosity, liquid-gas surface tension, initial impact velocity, droplet diameter, and the equilibrium contact angle with the surface. Table III details the standard values for these properties and the range over which each was varied during the simulations. FIG. 8 presents the results of the sensitivity analysis, showing normalized values of maximum spreading diameter (β_m), spreading time (t_s), contact time (t), and energy dissipation during spreading ($\bar{E}_{sdiss}$), each normalized relative to the standard case (see text box in FIG. 8a). These parameters were chosen since they are critical to the accuracy of analytical methods. For consistency and ease of comparison, all six figures maintain a constant y-axis range.

The effect of varying the equilibrium contact angle on impact dynamics is illustrated in FIG. 8(a). We varied the contact angle in increments of 2 degrees, to preserve the superhydrophobic nature of the surface and minimize any influence from contact angle hysteresis. As the equilibrium contact angle increases, making the surface more water-repellent, contact time initially decreases. However, at higher angles (e.g., $164-168^\circ$), the contact time remains (almost) constant. Spreading time, in contrast, consistently increases with larger θ_{eq}, while the maximum spreading radius decreases. Generally, increasing the equilibrium contact angle reduces the pinning force at the TPCL, thereby lowering the energy dissipated in that region[48]. Our results indicate that, while the energy dissipation during spreading varies within a $\pm 0.5\%$ range of the standard case when the equilibrium contact angle is increased from 156° to 166°, it decreases by approximately 2.5% when the equilibrium contact angle is 168°. We introduce a quadratic correlation to describe the dependence of energy dissipation during spreading on the equilibrium contact angle for a superhydrophobic surface with negligible contact angle hysteresis:

$$\frac{\bar{E}_{sdiss}}{\bar{E}_{sdiss,ref}} = -12.2\left(\frac{\theta_{eq}}{\theta_{eq,ref}}\right)^2 + 24.1\left(\frac{\theta_{eq}}{\theta_{eq,ref}}\right) - 11.0 \quad (17)$$

Note that in our simulations, we did not consider the effect of contact angle hysteresis, as it was minimal for superhydrophobic surfaces. However, the effect of contact angle hysteresis should be considered for hydrophobic or hydrophilic surfaces, where the pinning force at the TPCL is significant.

FIG.8(b) illustrates the effect of initial impact velocity on impact dynamics. The normalized maximum spreading diameter increases linearly with impact velocity, driven by the greater kinetic energy that promotes droplet spreading on the surface. Conversely, spreading time decreases with increasing impact velocity, as higher initial kinetic energy increases the spreading velocity, reducing the time needed for spreading. This observation aligns with the analytical model proposed by Pasandideh-Fard et al., which states that the spreading time is inversely proportional to the impact velocity[40]. Simulations indicate that at an initial velocity of 0.2 m/s, the droplet adheres to the surface due to insufficient kinetic energy for complete retraction. At 0.5 m/s, however, full rebound occurs, allowing contact time measurements. When the impact velocity is increased from 0.5 m/s to 1.4 m/s, the contact time remains independent of the impact velocity, which is consistent with models proposed in the literature[63,68]. However, a further increase in the impact velocity results in a slight reduction in contact time. Increasing the impact velocity also results in an increase in energy dissipation during the impact. The results on the effect of impact velocity on maximum spreading clearly show that with higher impact velocities, the droplet spreads more extensively on the solid surface, and this additional spreading is a source of energy dissipation. Additionally, larger and faster deformations of the liquid-gas interface lead to larger velocity gradients within the liquid medium and thus higher energy dissipation, consistently with Equations (4) and (5). Here, we propose an empirical correlation for the dependence of normalized energy dissipation during spreading on normalized impact velocity:

$$\frac{\bar{E}_{sdiss}}{\bar{E}_{sdiss,ref}} = 0.3\left(\frac{U}{U_{ref}}\right)^2 + 0.7\left(\frac{U}{U_{ref}}\right) \quad (18)$$

The influence of surface tension on impact dynamics is shown in FIG. 8(c). All observed parameters decrease as surface tension increases. Higher surface tension stores more surface energy during spreading, thus providing greater restoring force for droplet retraction and resulting in shorter contact and spreading times. The reduction of contact time with increasing surface tension is also in agreement with models in the literature[63,68]. Additionally, the reduction in spreading time with increasing liquid-gas surface tension is consistent with the empirical equation for spreading time, $t_s/(\rho {D_m}^3/8\gamma_{lv})^{1/2} = 0.92\,\mathrm{We}^{-0.43}$, proposed by Lin et al.[59]. Additionally, surface tension resists droplet spreading, leading to a reduction in maximum spreading diameter and time. Higher surface tension also restricts recirculation and surface interactions during spreading, thereby lowering overall energy dissipation. We present an empirical quadratic relationship to describe the dependence of normalized energy dissipation during spreading on normalized surface tension:

$$\frac{\bar{E}_{sdiss}}{\bar{E}_{sdiss,ref}} = 0.9\left(\frac{\gamma_{lv}}{\gamma_{lv,ref}}\right)^2 - 3.0\left(\left(\frac{\gamma_{lv}}{\gamma_{lv,ref}}\right) + 3.0\right. \quad (19)$$

This correlation also be explained using the mass-spring-damper model shown in FIG. 5. Increasing the stiffness of the spring (i.e., the surface tension) results in an increase in the natural frequency ($\omega_n = \sqrt{k_{eff}/m_{eff}}$), speeding up the dynamics of the model (droplet), and shortening the period of oscillation (i.e., the attainment of maximum deflection). Additionally, it can be shown that for a higher value of stiffness,

TABLE III. Parameters considered for the sensitivity analysis

	θ_{eq} (°)	U ($\frac{m}{s}$)	γ ($\frac{N}{m}$)	μ ($\frac{\text{kg}}{\text{m.s}}$)	D_0 (m)	ρ ($\frac{kg}{m^3}$)
Standard case values	162	1.4	0.072	9.74×10^{-4}	$2.23\times10^{-}3$	999.13
Range of change	$156-168$	$0.2-2.0$	$70\%-130\%$	$70\%-130\%$	$70\%-130\%$	$70\%-130\%$

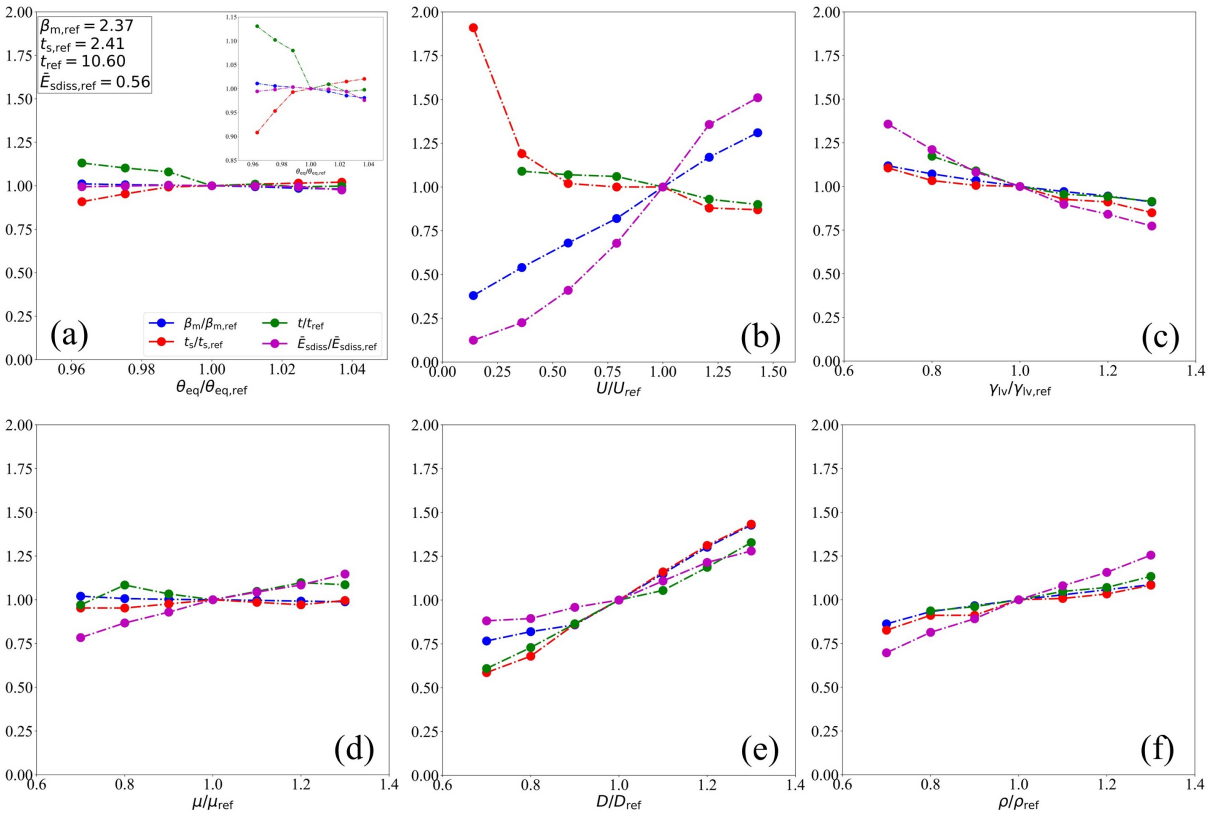

FIG. 8. Sensitivity analysis of the impact of various physiochemical properties on maximum spreading ratio, spreading time, contact time, and normalized energy dissipation during the spreading

the amplitude of free vibration (in our analogy this is the maximum spreading diameter) is lower[69]. Reduction in damping ratio ($\zeta = c_{eff}/(2\sqrt{m_{eff}k_{eff}})$), and consequently reduction in energy dissipation, is another outcome of the increase in stiffness.

The effect of liquid viscosity on impact dynamics, depicted in FIG. 8(d), is primarily observed in energy dissipation during spreading. While viscosity has minimal influence on maximum spreading diameter, contact time, and spreading time, energy dissipation increases linearly with higher viscosity. Specifically, an 85% increase in viscosity yields a 45% rise in energy dissipation, while contact time decreases by approximately 12.5%. The linear dependence of normalized energy dissipation during spreading on normalized viscosity can be described by:

$$\frac{\bar{E}_{sdiss}}{\bar{E}_{sdiss,ref}} = 0.6\left(\frac{\mu}{\mu_{ref}}\right) + 0.4 \tag{20}$$

In the mass-spring-damper model of the droplet, the viscosity of the liquid plays a key role in energy dissipation via a linear relationship. This can be shown by the Rayleigh dissipation function ($D = \frac{1}{2}c\dot{x}^2$), where c is the damping coefficient. In this function, the dissipated energy is linearly proportional to the damping coefficient[70]. Additionally, increasing the viscosity (i.e., damping coefficient in the mass-spring-damper model) leads to a reduction in the damped natural frequency of the system, which may slow it down and increase the oscillation period. However, in free vibrations, the damping ratio affects the amplitude of vibration as well ($X \propto \zeta^{1/2}$). The time to reach maximum deflection for a mass-spring-damper system in free vibration can be determined by:

$$t_{max} = \frac{\arctan(\frac{\sqrt{1-\zeta^2}}{\zeta}) - \phi}{\omega_d} \tag{21}$$

where

$$\omega_d = \omega_n\sqrt{1-\zeta^2}, \omega_n = \sqrt{\frac{k_{eff}}{m_{eff}}}, \phi = \arctan\left(\frac{x_0\omega_d}{v_0+\zeta\omega_n x_0}\right) \tag{22}$$

where x_0 and v_0 are the initial displacement and velocity of the oscillator, respectively. Equation (21) shows that increasing the damping ratio in a single-degree-of-freedom system results in a slight reduction in the time until maximum deflection (i.e., maximum spreading for a droplet). This can be easily extended to higher degrees of freedom, which proves the observation from this study.

Finally, FIGs 8(e) and 8(f) illustrate the impact of droplet size and density on the parameters of interest. All parameters increase with both droplet density and size, demonstrating a proportional relationship with these properties which is in agreement with empirical models proposed in the literature[59,68,71]. The concept of a mass-spring-damper system supports this observation. For example, Equation 21 proves that increasing the mass would increase the maximum deflection (spreading) time. On the other hand, increasing both density and droplet size increases the mass. Hence, it can be shown that the maximum deflection δ_{max} increases by increasing the mass:

$$\delta_{max} = \frac{1}{\omega_d}\sqrt{(v_0+\zeta\omega_n x_0)^2 + (x_0\omega_d)^2}, \tag{23}$$

This is in accordance with the results shown in FIG. 8(e) and 8(f).

FIG. 9 demonstrates the performance of the CFD simulation in predicting maximum spreading in comparison to the maximum spreading calculated using the correlations proposed by Pasandideh-Fard et al.[40], Clanet et al.[41], and Aksoy et al.[44]. Various shapes are used in FIG. 9 to distinguish the effects of different parameters. The results indicate that, for the majority of cases, the discrepancy between the CFD results of this study and the models from the literature is less than 20%. However, the difference becomes more pronounced for the effect of droplet diameter when $Re^2.Oh$ is high. This is attributable to the presence of more internal recirculations and increased maximum spreading, which renders the assumption of zero kinetic energy at maximum spreading less applicable. This figure confirms the reliability of our model in predicting maximum spreading using CFD results.

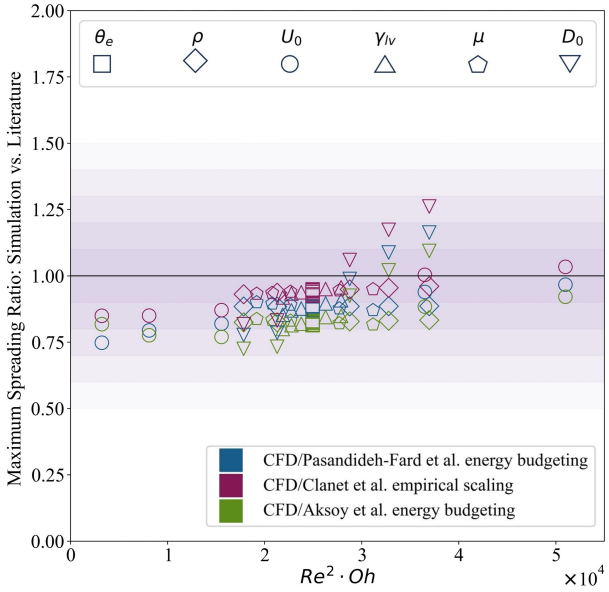

FIG. 9. Performance of some of analytical models presented in Table I compared to our CFD results. The results from different studies are coded with different colors and compared to our results. Different shapes

V. CONCLUSIONS

Numerous analytical models have been proposed in the literature to estimate the characteristic parameters of droplet impact, but their accuracy is heavily dependent on the assumptions made during their derivation or the experimental data used. To provide detailed information on the energy budget of the droplet during the impact, in this study, we utilized a VOF-based CFD model to precisely simulate droplet impact phenomena, capturing detailed impact dynamics during the spreading and recoil phases. An extensive CFD simulation campaign was conducted, comprising 37 simulations. Each parallel simulation required between 36 and 54 hours on a high-performance computing (HPC) system. Following mesh independence tests and model validation against experimental results, we analyzed the energy budget of droplet impact and proposed a simple mass-spring-damper model to explain the energy transfer mechanisms during the impact. Using the capabilities of CFD simulations, we systematically varied one parameter at a time while keeping all other parameters constant. This approach allowed us to isolate and analyze the effect of each parameter independently on impact dynamics and energy budget. The results from this study offer valuable insights that can aid researchers in developing more accurate analytical or empirical models in the future.

AUTHOR DECLARATIONS

Conflict of Interest

The authors have no conflicts to disclose.

Data Availability Statement

The data that support the findings of this study are available from the corresponding author upon reasonable request.

ACKNOWLEDGMENTS

The authors would like to thank Francois De Luca and Dave Ions for fruitful discussions.

REFERENCES

[1] W. L. Ng, X. Huang, V. Shkolnikov, G. L. Goh, R. Suntornnond, and W. Y. Yeong, "Controlling Droplet Impact Velocity and Droplet Volume: Key Factors to Achieving High Cell Viability in Sub-Nanoliter Droplet-based Bioprinting," International Journal of Bioprinting **8**, 1–17 (2022).

[2] X. Dong, G. Hao, and Y. Liu, "Efficient mesh-free modeling of liquid droplet impact on elastic surfaces," Engineering with Computers **39**, 3441–3471 (2023).

[3] S. A. Kulinich and M. Farzaneh, "How wetting hysteresis influences ice adhesion strength on superhydrophobic surfaces," Langmuir **25**, 8854–8856 (2009).

[4] H. Wang, H. Lu, and W. Zhao, "A review of droplet bouncing behaviors on superhydrophobic surfaces: Theory, methods, and applications," Physics of Fluids **35**, 21301 (2023).

[5] H. H. Singh and N. Khare, "A ferroelectric nanocomposite-film-based device for harvesting energy from water droplets using both piezoelectric and triboelectric effects," Nanotechnology **32** (2021), 10.1088/1361-6528/ac171b.

[6] A. Albadi and Y. Zhang, "Experimental study of water droplet impact on burning wood surfaces," Proceedings of the Combustion Institute **38**, 4605–4613 (2021).

[7] A. M. Worthington, "XXVIII. On the forms assumed by drops of liquids falling vertically on a horizontal plate," Proceedings of the Royal Society of London **25**, 261–272 (1877).

[8] A. L. Yarin, "Drop impact dynamics: Splashing, spreading, receding, bouncing.." Annual Review of Fluid Mechanics **38**, 159–192 (2006).

[9] C. Josserand and S. T. Thoroddsen, "Drop Impact on a Solid Surface," Annual Review of Fluid Mechanics **48**, 365–391 (2016).

[10] G. McHale, "Cassie and Wenzel: Were they really so wrong?" Langmuir **23**, 8200–8205 (2007).

[11] D. Khojasteh, M. Kazerooni, S. Salarian, and R. Kamali, "Droplet impact on superhydrophobic surfaces: A review of recent developments," Journal of Industrial and Engineering Chemistry **42**, 1–14 (2016).

[12] Y. C. Jung and B. Bhushan, "Dynamic effects of bouncing water droplets on superhydrophobic surfaces," Langmuir **24**, 6262–6269 (2008).

[13] X. Li, X. Ma, and Z. Lan, "Dynamic behavior of the water droplet impact on a textured hydrophobic/superhydrophobic surface: The effect of the remaining liquid film arising on the pillars' tops on the contact time," Langmuir **26**, 4831–4838 (2010).

[14] L. Xu, "Liquid drop splashing on smooth, rough, and textured surfaces," Physical Review E - Statistical, Nonlinear, and Soft Matter Physics **75**, 056316 (2007).

[15] M. H. Biroun, L. Haworth, P. Agrawal, B. Orme, G. McHale, H. Torun, M. Rahmati, and Y. Q. Fu, "Surface Acoustic Waves to Control Droplet Impact onto Superhydrophobic and Slippery Liquid-Infused Porous Surfaces," ACS Applied Materials and Interfaces **13**, 46076–46087 (2021).

[16] C. D. Modak, A. Kumar, A. Tripathy, and P. Sen, "Drop impact printing," Nature Communications **11**, 1–11 (2020).

[17] J. E. Stringer, P. J. Smith, and B. Derby, "Droplet behaviour in inkjet printing," Materials Research Society Symposium Proceedings **860**, 1–6 (2004).

[18] K. Boos, A. Orr, M. Illes, and T. Stotesbury, "Characterizing drip patterns in bloodstain pattern analysis: An investigation of the influence of droplet impact velocity and number of droplets on static pattern features," Forensic Science International **301**, 55–66 (2019).

[19] F. Geyer, M. DAcunzi, A. Sharifi-Aghili, A. Saal, N. Gao, A. Kaltbeitzel, T. F. Sloot, R. Berger, H. J. Butt, and D. Vollmer, "When and how self-cleaning of superhydrophobic surfaces works," Science Advances **6** (2020), 10.1126/sciadv.aaw9727.

[20] W. Jia and H. H. Qiu, "Experimental investigation of droplet dynamics and heat transfer in spray cooling," Experimental Thermal and Fluid Science **27**, 829–838 (2003).

[21] S. Chandra and C. T. Avedisian, "On the collision of a droplet with a solid surface," Proceedings of the Royal Society A: Mathematical, Physical and Engineering Sciences **432**, 13–41 (1991).

[22] M. H. Biroun, L. Haworth, H. Abdolnezhad, A. Khosravi, P. Agrawal, G. McHale, H. Torun, C. Semprebon, M. Jabbari, and Y. Q. Fu, "Impact Dynamics of Non-Newtonian Droplets on Superhydrophobic Surfaces," Langmuir **39**, 5793–5802 (2023).

[23] M. Jadidi, J. Y. Trepanier, M. A. Farzad, and A. Dolatabadi, "Effects of ambient air relative humidity and surface temperature on water droplet spreading dynamics," American Society of Mechanical Engineers, Fluids Engineering Division (Publication) FEDSM **1** (2018), 10.1115/FEDSM2018-83287.

[24] C. Christodoulou, E. Sorensen, S. García-Muñoz, and L. Mazzei, "Mathematical modelling of water absorption and evaporation in a pharmaceutical tablet during film coating," Chemical Engineering Science **175**, 40–55 (2018).

[25] R. Rioboo, M. Marengo, and C. Tropea, "Time evolution of liquid drop impact onto solid, dry surfaces," Experiments in Fluids **33**, 112–124 (2002).

[26] A. Ahmed, A. J. Qureshi, B. A. Fleck, and P. R. Waghmare, "Effects of magnetic field on the spreading dynamics of an impinging ferrofluid droplet," Journal of Colloid and Interface Science **532**, 309–320 (2018).

[27] X. Liu, X. Zhang, and J. Min, "Maximum spreading of droplets impacting spherical surfaces," Physics of Fluids **31**, 92102 (2019).

[28] M. H. Biroun, J. Li, R. Tao, M. Rahmati, G. McHale, L. Dong, M. Jangi, H. Torun, and Y. Q. Fu, "Acoustic waves for active reduction of contact time in droplet impact," Physical Review Applied **14**, 024029 (2020).

[29] J. Eggers, M. A. Fontelos, C. Josserand, and S. Zaleski, "Drop dynamics after impact on a solid wall: Theory and simulations," Physics of Fluids **22** (2010), 10.1063/1.3432498.

[30] I. V. Roisman, "Inertia dominated drop collisions. II. An analytical solution of the Navier-Stokes equations for a spreading viscous film," Physics of Fluids **21** (2009), 10.1063/1.3129283.

[31] N. Laan, K. G. De Bruin, D. Bartolo, C. Josserand, and D. Bonn, "Maximum diameter of impacting liquid droplets," Physical Review Applied **2** (2014), 10.1103/PhysRevApplied.2.044018.

[32] J. B. Lee, N. Laan, K. G. De Bruin, G. Skantzaris, N. Shahidzadeh, D. Derome, J. Carmeliet, and D. Bonn, "Universal rescaling of drop impact on smooth and rough surfaces," Journal of Fluid Mechanics **786**, R41–R411 (2015).

[33] R. Choudhury, D. M. T. Nasir, D. R. Kaiser, R. Ghimire, D. A. Aliyu, D. B. Sohani, D. J. Atanbori, D. R. Rathaur, and D. R. Mishra, "Uncovering the Effect of Physical Conditions and Surface Roughness on the Maximum Spreading Factor of Impinging Droplets Using a Supervised Artificial Neural Network Model," Industrial and Engineering Chemistry Research **62**, 21208–21221 (2023).

[34] L. Au-Yeung and P. A. Tsai, "Predicting Impact Outcomes and Maximum Spreading of Drop Impact on Heated Nanostructures Using Machine Learning," Langmuir **39**, 18327–18341 (2023).

[35] J. B. Lee, D. Derome, A. Dolatabadi, and J. Carmeliet, "Energy Budget of Liquid Drop Impact at Maximum Spreading: Numerical Simulations and Experiments," Langmuir **32**, 1279–1288 (2016).

[36] F. Wang, L. Yang, L. Wang, Y. Zhu, and T. Fang, "Maximum Spread of Droplet Impacting onto Solid Surfaces with Different Wettabilities: Adopting a Rim-Lamella Shape," Langmuir **35**, 3204–3214 (2019).

[37] H. M. Huang and X. P. Chen, "Energetic analysis of drop's maximum spreading on solid surface with low impact speed," Physics of Fluids **30**, 22106 (2018).

[38] H. K. Huh, S. Jung, K. W. Seo, and S. J. Lee, "Role of polymer concentration and molecular weight on the rebounding behaviors of polymer solution droplet impacting on hydrophobic surfaces," Microfluidics and Nanofluidics **18**, 1221–1232 (2015).

[39] B. L. Scheller and D. W. Bousfield, "Newtonian drop impact with a solid surface," AIChE Journal **41**, 1357–1367 (1995).

[40] M. Pasandideh-Fard, Y. M. Qiao, S. Chandra, and J. Mostaghimi, "Capillary effects during droplet impact on a solid surface," Physics of Fluids **8**, 650–659 (1996).

[41] C. Clanet, C. Béguin, D. Richard, and D. Quéré, "Maximal deformation of an impacting drop," Journal of Fluid Mechanics **517**, 199–208 (2004).

[42] C. Ukiwe and D. Y. Kwok, "On the maximum spreading diameter of impacting droplets on well-prepared solid surfaces," Langmuir **21**, 666–673

(2005).
[43]J. Seo, J. S. Lee, H. Y. Kim, and S. S. Yoon, "Empirical model for the maximum spreading diameter of low-viscosity droplets on a dry wall," Experimental Thermal and Fluid Science **61**, 121–129 (2015).
[44]Y. T. Aksoy, P. Eneren, E. Koos, and M. R. Vetrano, "Spreading of a droplet impacting on a smooth flat surface: How liquid viscosity influences the maximum spreading time and spreading ratio," Physics of Fluids **34**, 42106 (2022).
[45]J. Du, X. Wang, Y. Li, Q. Min, and X. Wu, "Analytical Consideration for the Maximum Spreading Factor of Liquid Droplet Impact on a Smooth Solid Surface," Langmuir **37**, 7582–7590 (2021).
[46]H. Liu, J. Chen, and J. Wang, "A universal rescaling law for the maximum spreading factor of non-Newtonian droplets with power-law fluids," (2024).
[47]I. V. Roisman, L. Opfer, C. Tropea, M. Raessi, J. Mostaghimi, and S. Chandra, "Drop impact onto a dry surface: Role of the dynamic contact angle," Colloids and Surfaces A: Physicochemical and Engineering Aspects **322**, 183–191 (2008).
[48]M. H. Biroun, M. Rahmati, R. Tao, H. Torun, M. Jangi, and Y. Fu, "Dynamic Behavior of Droplet Impact on Inclined Surfaces with Acoustic Waves," Langmuir **36**, 10175–10186 (2020).
[49]J. Yao, J. Wang, H. Xu, L. Zuo, B. Li, and Q. Dong, "Lattice Boltzmann study of droplet dynamic behaviors impinging on textured surfaces under an external electric field," Physics of Fluids **36** (2024), 10.1063/5.0219922/3309113.
[50]M. S. Ambrosia, J. Jang, and M. Y. Ha, "Static and dynamic hydrophobicity on a nano-sized groove/ridge surface," Computers & Fluids **114**, 75–83 (2015).
[51]M. H. Biroun, M. T. Rahmati, M. Jangi, R. Tao, B. X. Chen, and Y. Q. Fu, "Computational and experimental analysis of droplet transportation/jetting behaviours driven by thin film surface acoustic waves," Sensors and Actuators, A: Physical **299**, 111624 (2019).
[52]H. Chen, S. Chen, and W. H. Matthaeus, "Recovery of the Navier-Stokes equations using a lattice-gas Boltzmann method," Physical Review A **45**, R5339 (1992).
[53]T. Koishi, K. Yasuoka, and X. C. Zeng, "Molecular Dynamics Simulation of Water Nanodroplet Bounce Back from Flat and Nanopillared Surface," Langmuir **33**, 10184–10192 (2017).
[54]H. Li and K. Zhang, "Dynamic behavior of water droplets impacting on the superhydrophobic surface: Both experimental study and molecular dynamics simulation study," Applied Surface Science **498**, 143793 (2019).
[55]T. Koishi, K. Yasuoka, S. Fujikawa, and X. C. Zeng, "Measurement of contact-angle hysteresis for droplets on nanopillared surface and in the Cassie and Wenzel states: A molecular dynamics simulation study," ACS Nano **5**, 6834–6842 (2011).
[56]J. J. Derksen and A. E. Komrakova, "Multiscale simulations of sliding droplets," Acta Mechanica **230**, 657–666 (2019).
[57]J. Zhang, M. K. Borg, and J. M. Reese, "Multiscale simulation of dynamic wetting," (2017), 10.1016/j.ijheatmasstransfer.2017.07.034.
[58]T. Qian, X. P. Wang, and P. Sheng, "A variational approach to moving contact line hydrodynamics," Journal of Fluid Mechanics **564**, 333–360 (2006).
[59]S. Lin, B. Zhao, S. Zou, J. Guo, Z. Wei, and L. Chen, "Impact of viscous droplets on different wettable surfaces: Impact phenomena, the maximum spreading factor, spreading time and post-impact oscillation," Journal of Colloid and Interface Science **516**, 86–97 (2018).
[60]C. Hao, Y. Liu, X. Chen, J. Li, M. Zhang, Y. Zhao, and Z. Wang, "Bioinspired Interfacial Materials with Enhanced Drop Mobility: From Fundamentals to Multifunctional Applications," Small **12**, 1825–1839 (2016).
[61]G. Liang, Y. Chen, L. Chen, and S. Shen, "Maximum Spreading for Liquid Drop Impacting on Solid Surface," Industrial and Engineering Chemistry Research **58**, 10053–10063 (2019).
[62]J. B. Lee, D. Derome, R. Guyer, and J. Carmeliet, "Modeling the Maximum Spreading of Liquid Droplets Impacting Wetting and Nonwetting Surfaces," Langmuir **32**, 1299–1308 (2016).
[63]D. Richard, C. Clanet, and D. Quéré, "Surface phenomena: Contact time of a bouncing drop," Nature **417**, 811 (2002).
[64]"The Open Source CFD Toolbox User Guide," (2016).
[65]C. W. Hirt and B. D. Nichols, "Volume of fluid (VOF) method for the dynamics of free boundaries," Journal of Computational Physics **39**, 201–225 (1981).
[66]. Šikalo, H. D. Wilhelm, I. V. Roisman, S. Jakirlić, and C. Tropea, "Dynamic contact angle of spreading droplets: Experiments and simulations," Physics of Fluids **17**, 1–13 (2005).
[67]K. Yokoi, D. Vadillo, J. Hinch, and I. Hutchings, "Numerical studies of the influence of the dynamic contact angle on a droplet impacting on a dry surface," Physics of Fluids **21**, 1–12 (2009).
[68]M. Abolghasemibizaki, N. Dilmaghani, R. Mohammadi, and C. E. Castano, "Viscous Droplet Impact on Nonwettable Textured Surfaces," Langmuir **35**, 10752–10761 (2019).
[69]R. C. Hibbeler and S. C. Fan, "Engineering mechanics : dynamics," , 688 (2004).
[70]J. Taghipour, M. Dardel, and M. H. Pashaei, "Vibration mitigation of a nonlinear rotor system with linear and nonlinear vibration absorbers," Mechanism and Machine Theory **128**, 586–615 (2018).
[71]Y. Fan, Y. Tan, Y. Dou, S. Huang, and X. Tian, "Reducing the contact time of bouncing droplets on superhydrophobic surfaces: Foundations, strategies and applications," Chemical Engineering Journal **476**, 146485 (2023).